



## Construction and Characterization of an Indoor Smog Chamber for the Measurement of the Optical and Physicochemical Properties of Aging Biomass Burning Aerosols Native to sub-Saharan Africa

5 **Damon M. Smith,<sup>1</sup> Marc N. Fiddler,<sup>2</sup> Kenneth G. Sexton<sup>3</sup> and Solomon Bililign<sup>2,4</sup>**

<sup>1</sup>Energy and Environmental Systems Department, North Carolina A&T State University, Greensboro, North Carolina, USA

<sup>2</sup>NOAA-ISET Center, North Carolina A&T State University, Greensboro, North Carolina, USA

10 <sup>3</sup>Department of Environmental Sciences and Engineering, Gillings School of Global Public Health, University of North Carolina at Chapel Hill, NC, USA

<sup>4</sup>Department of Physics, North Carolina A&T State University, Greensboro, North Carolina, USA

*Correspondence to:* Solomon Bililign [bililignsol@gmail.com](mailto:bililignsol@gmail.com)

15

**Abstract.** We describe here the construction and characterization of a new smog chamber facility (NCAT chamber) for studying the chemical and optical properties of biomass burning (BB) aerosols from biomass fuels native to sub-Saharan Africa. This facility is comprised of a  $\sim 9$  m<sup>3</sup> fluorinated ethylene propylene film (FEP) reactor placed in a temperature-controlled room and coupled with a cavity ring-down spectrometer, nephelometer, 20 condensation particle counter, differential mobility analyzer and other analytical instruments, such as NO<sub>x</sub> and O<sub>3</sub> analyzers, a GC, a filter sampler, and an impinger for collecting particles in water. Construction details and characterization experiments are described, including measurements of BB particulate size distribution and deposition rate, gas wall loss rates, dilution rate, light intensity, mixing speed, temperature and humidity variations, and air purification method. The wall loss rates for NO, NO<sub>2</sub>, and O<sub>3</sub> were found to be  $(7.40 \pm 0.01) \times 10^{-4}$ ,  $(3.47 \pm 25 0.01) \times 10^{-4}$ , and  $(5.90 \pm 0.08) \times 10^{-4} \text{ min}^{-1}$  respectively. The NO<sub>2</sub> photolysis rate constant was  $0.165 \pm 0.005 \text{ min}^{-1}$ , which corresponds to a flux of  $(7.72 \pm 0.25) \times 10^{17} \text{ photons} \cdot \text{nm} \cdot \text{cm}^{-2} \cdot \text{s}^{-1}$  from 296.0–516.8 nm. Particle deposition rate was found to be  $(2.46 \pm 0.11) \times 10^{-3} \text{ min}^{-1}$  for pine at  $D_p = 100$  nm. After initial mixing in the chamber, with the ultraviolet (UV) light off, the particle size distribution for BB samples used for the initial work did not stabilize until 30  $\sim 7.5$  hours after injection peaking near a mobility diameter of  $\sim 340$  nm. The chamber demonstrated gas and particle loss rates, and other properties comparable to other similar indoor smog chambers

### 1. Introduction

Biomass burning (BB) is one of the largest sources of black carbon (BC), or absorbing aerosols, in the atmosphere, with as much as 30 % of aerosol mass belonging to BC (Andreae et al., 1998; Moosmüller et al., 2009; Bond et al., 2013). It is important to study BB aerosols because of their impact on air quality, cloud formation, 35 human health, and climate. While it is well known that BB aerosols contribute to climate forcing, much is still unknown about the extent of this forcing, owing to the high level of uncertainty regarding BB aerosol optical properties (Andreae and Merlet, 2001; Koch et al., 2009; IPCC, 2013). This uncertainty is partially due to the difficulty in quantifying the amount of light absorption and scattering by aerosols, which depends on their size,



40 chemical composition, age, humidity, and the wavelength of incident light (Harvey et al., 2016; Kim and Paulson, 2013; Kanakidou et al., 2005).

Biomass burning is a global phenomenon and the contribution of biomass burning aerosols in the atmosphere is the highest in the tropics (Shi et al., 2015). While the optical properties of BB aerosols produced by several North American biomass fuels have been and are being investigated, both in the laboratory and in field campaigns (Hodzic et al., 2007; Yokelson et al., 2009; Liu et al., 2014; McMeeking et al., 2009; Levin et al., 45 2010; Mack, 2008; Mack et al., 2010), BB aerosols for sub-Saharan African fuels were only investigated in field studies (Liousse et al., 2010; Formenti et al., 2003). To our knowledge, there have not been any laboratory studies of the optical properties of BB aerosols from fuels sources common in sub-Saharan Africa. Africa is the single largest continental source of BB emissions, with sub-Saharan Africa hosting some of the highest levels of atmospheric black and brown carbon (BrC) aerosols. Some studies estimate around 55 % of the global contributions to BB 50 aerosols come from Africa (Ichoku et al., 2008; Roberts and Wooster, 2008; Roberts et al., 2009; Lamarque et al., 2010; van der Werf et al., 2010; Schultz et al., 2008).

There have been several studies on the physicochemical properties of BB particles in ambient investigations. Diameters and chemical compositions of wood-fire particles have been shown to change rapidly during the daytime, where photochemical oxidation increased the organic aerosol (OA) fraction (Zauscher et al., 55 2013). The cloud condensation nuclei (CCN) activity was found to be impaired by photochemistry (Engelhart et al., 2012; Giordano and Asa-Awuku, 2014). What happens to smoke particles in the absence of light and increased relative humidity (RH) is not yet clear (Murphy et al., 2006) and dynamic influence of humidity on the evolution of smoke particles is not defined (Li et al., 2015). Humidity may also change the physicochemical properties of aerosol during aging (Rubasinghege and Grassian, 2013). Understanding daytime and nighttime aging under the high RH 60 conditions that are typical in the tropics is clearly needed. The influence of combustion properties, such as fire characteristics, burning stage, fuel type, and meteorological conditions on optical properties of BB aerosols for the region is also important.

The total mass of atmospheric aerosol is dominated by OA (20–90 %) and is composed primarily of secondary organic aerosol (SOA) (Zhang et al., 2011; Kanakidou et al., 2005; Jimenez et al., 2009; Gentner et al., 65 2017), which are produced from the atmospheric oxidation and processing of volatile organic compounds (VOCs) (Robinson et al., 2007; Gentner et al., 2012). A smaller fraction of OA is directly emitted as primary organic aerosol (POA) (Hallquist et al., 2009).

Quantifying the effects of net SOA formation and aging from BB smoke in the field poses a challenge because of variability between studies, due to different gas- and particle-phase emissions from different fuel types, 70 burning conditions, external mixing of other aerosol types, and other environmental factors present in the region of smoke emission. A critical element of this uncertainty relates to the evolution of aerosol loadings within the atmosphere. In addition to an increase in overall aerosol loadings, secondary aerosol formation also acts to increase the single scattering albedo (SSA) of BB aerosol (Yokelson et al., 2009; Reid et al., 1998; Abel et al., 2003), potentially changing its climate forcing from a net warming effect to a net cooling effect. While SOA formation 75 leading to a significant enhancement of OA mass has been widely observed in anthropogenic urban emissions, the



net contribution in aging biomass burning plumes remains unclear (De Gouw and Jimenez, 2009; Hawkins and Russell, 2010).

Laboratory studies are clearly needed to measure the optical properties of BB aerosols from African fuel sources as they age and interact with polluted air that has the same chemical profile as African mega cities. Smog chambers provide a controlled environment to study the formation and the evolution of specific compounds and particles produced from specific fuel sources of interest by isolating the influence of emissions, meteorology, and mixing effects.

Smog chambers (both indoor and outdoor) have been used, beginning in the 1960s, to study atmospheric processes in controlled environments, such as biomass burning emissions (Kamens et al., 1984; Hennigan et al., 2011; Bian et al., 2015), SOA production (Carter et al., 2005; Babar et al., 2016), diesel exhaust (Weitkamp et al., 2007), and cigarette smoke (Schick et al., 2012). As opposed to in situ measurements, the aging process can be studied over longer times in a chamber with greater temporal accuracy and sampling frequency.

Construction of smog chamber (inner reactor) walls can use a variety of materials, such as stainless steel (Akimoto et al., 1979; Wang et al., 2011) and Teflon FEP film (Cocker et al., 2001; Carter et al., 2005; Babar et al., 2016). FEP film is the most widely used for large chamber designs due to its transparency in the ultraviolet (UV) spectrum, flexibility under changes in pressure, chemical inertness, and economic feasibility (Wang et al., 2014; Wu et al., 2007). While outdoor chambers provide the most realistic conditions when it comes to the solar spectrum, repeatability of experiments is poor, with too many changing variables dependent on the time of year, angle of the sun in the sky, and other weather conditions. Indoor chambers have the advantage of temperature and humidity controls, as well as consistent light intensity (Babar et al., 2016). Modern ultraviolet bulbs, while not having the same spectra as solar light, can be characterized to create accurate models of atmospheric conditions. However, it is also worth noting that the difference in artificial light spectrum and solar spectrum may lead to different photolysis rates for some reactions (Carter et al., 2005; Takekawa et al., 2003).

In this paper, we describe construction and characterization of an indoor smog chamber built in our laboratory at North Carolina A&T State University (hereafter referred to as NCAT Chamber) to study the optical and physicochemical properties of BB aerosols produced by fuel sources from sub-Saharan Africa. While studying these fuels is the goal of this facility, this paper will present work on white pine to facilitate a comparison with similar chambers. In addition to details of the construction and characterization experiments we describe how BB aerosols are produced and introduced into the chamber and how the aerosols are sampled for measuring their broadband optical properties (absorption, extinction, and scattering) as a function of particle size and age.

## 2. Description of chamber and optical properties measurement facility

### 2.1. Chamber facility

The NCAT Chamber is located on one end of our 175 m<sup>3</sup> lab, on the opposite side of the room from the vents connected to the building's HVAC system. The chamber is placed as close as possible to test mixture preparation sources (tube furnace and gas cylinders) and monitoring instruments to minimize injection and sample line losses, while allowing room for chamber operators to move between the chamber and surrounding instruments.



115

Mixture preparation sources are located inside or near laboratory hoods. Typical lab temperature is between 17 and 21 °C, with relative humidity between 30 % and 60 %. Under normal operating conditions, the chamber can remain near 0% humidity (below the detection limits of our instrument) with only minimal purge flow needed to obtain a small positive pressure (balanced against air sampling requirements), having temperatures close to room temperature while the UV lights are off. With no flows to or from the chamber, humidity increases from near 0 % to under 7 % after 24 hours.

## 2.2. Chamber construction

120

125

130

135

140

The chamber system is composed of two parts: the inner reactor and the outer frame. The reactor is made of 12 rectangular frames connected by hex bolts to form a box having inner dimensions (length × width × height) of 2.36 m × 1.85 m × 2.06 m, for a volume ~9 m<sup>3</sup>. Each frame is made of wood (having a cross section of 1.5 in by 1.5 in) and wrapped in fluorocarbon film (DuPont, type 500A FEP100, 50-inch width, 125 μm thickness), which is secured by staples to the back of the wooden frame. The frames are attached to each other so that the inner surface of the reactor is completely covered by the FEP film, leaving all wood surfaces facing the exterior, while the FEP film itself is compressed between panels (using bolts approximately every six inches) to form an airtight seal. Some of the frames were reinforced by steel angle iron to straighten out the wood and provide a more rigid structure for the reactor. With this design, no heat-seals are necessary, which can be expensive and is prone to failure from flexing, which can result in leaking. With this design, the reactor was configured so that an individual panel could easily be detached from the chamber for either cleaning or repair. Cinder blocks are used to elevate the reactor to be centered against the outer frame and to allow for airflow under the reactor for even temperature distribution. Two smaller steel panels were attached to the wooden frames on opposite sides of the reactor, flush against the FEP film to support stainless steel bulkhead fittings for injection and sampling lines. The FEP film, again, served as a seal for these fittings. While the structure of the reactor is rigid, the FEP film walls are flexible, always maintaining nearly constant room pressure in the chamber. Although it is assumed that the chamber is airtight, it is more likely that there are small leaks in the chamber, which would allow room air to mix with chamber air. For this reason, the chamber is kept at a slight positive pressure during experiments to ensure that any leaks would be from the chamber into the room. In this way, chamber air does not become contaminated. Rising humidity in the chamber is one indication that room air is leaking into the chamber, due to the difference in relative humidity between chamber air and room air. If a leak becomes too large, or if the FEP film is punctured, the frame in question can be removed and repaired.

145

The outer frame of the chamber is made of steel angle iron, having dimensions (length × width × height) of 2.55 m × 2.45 m × 2.48 m, which is primarily used for mounting the UV lights and protective coverings. On each of two opposite sides of the chamber, there are two rows of eight light fixtures spaced evenly along the side of the chamber. Each fixture holds two bulbs (Sylvania, 30-watt UVA, 356 nm centered spectrum, F30T8/350BL/ECO, 36"), for a total of thirty-two bulbs to a side, or sixty-four bulbs for the chamber. Each side of the chamber (hereafter referred to as door side or window side, corresponding to the door and window of the laboratory) has been wired to a separate circuit with a light switch, allowing for irradiation using either 50 % or 100 % of the total light intensity



available. Due to the amount of space available in our lab, UV lamps are ~18 cm from the FEP film surface. Chamber temperature is elevated slightly during operation of the UV lamps and is described in more detail below.

150 Protective Masonite is attached to the outer frame on all sides of the chamber, including ceiling, except for two windows surrounding the injection and sampling panels which are left uncovered for visual inspection of the chamber and the floor where the Masonite is attached directly to the wooden frame of the reactor. The inner surface of the Masonite is covered with aluminum foil to reflect and scatter most of the light emitted from the UV lamps surrounding the chamber to simulate uniform irradiance.

### 155 **2.3. Air purification**

Room air can be drawn into the chamber through a 3-inch diameter PVC pipe, fitted with a dust filter to keep out contaminants and dust. The laboratory exhaust system is connected to the chamber via a check-valve and gated valve used as the exhaust port. This serves to evacuate the chamber with either the room air for primary flushing or with clean air for thorough chamber cleaning. This room air input is primarily used to quickly evacuate

160 the chamber after a burn has been completed. To generate clean air, compressed house air, having very low humidity, is passed through a 0.01  $\mu\text{m}$  activated carbon filter (Speedaire, 4GNN4), followed by a zero-air generator (Aadco Instruments, 747-30), and a ballast tank (Aadco Instruments). The generator is capable of a maximum flow rate of 30 L/min and removes any particulates, hydrocarbons,  $\text{NO}_x$ , and  $\text{SO}_x$  from the air, while the ballast tank's volume keeps pressure fluctuations, and, by extension, flow rate fluctuations, to a minimum. Gas purity is less than

165 1 ppb for  $\text{O}_3$  and CO and less than 0.5 ppb for  $\text{SO}_2$ ,  $\text{H}_2\text{S}$ , NO,  $\text{NO}_2$ ,  $\text{NH}_3$ , and both methane and non-methane hydrocarbons. Air flow to the chamber is controlled by a high-flow rotameter (Cole-Parmer EW-32033-16), which is capable of flow rates greater than 60 L/min and is used to balance flows going into the chamber with flows coming out of the chamber. Since the rigidity of the chamber frame keeps the FEP film walls from completely collapsing in on itself, flow rates going into and out of the chamber must remain balanced (or slightly positive, as

170 stated above). While zero-air is sent directly to the chamber after the ballast, air used for other systems is pressure regulated with a single stage regulator (Grainger, 4ZM13).

### **2.4. Gas and particle injection**

Additional gases, such as commercially prepared gas cylinders of NO and  $\text{NO}_2$ , in nitrogen can be injected via a second, low-flow rotameter (Cole-Parmer EW-32033-16) with a maximum flow of 1.25 L/min. Concentrations

175 can be calculated from timed injections, certified reagent gas concentration, flow-rate, and chamber volume. A three-way valve between the rotameter and chamber input can be set to exhaust, chamber, or off. In the exhaust position, the flow rate can reach equilibrium before switching to the chamber position, allowing for accurate measurement of injections if elapsed time is known. Other chemical compounds, such as aromatic hydrocarbons (high purity), can be injected in the liquid phase by syringe through a rubber stopper into a glass U-tube. If

180 necessary, these chemicals can be evaporated by heating the U-tube. A portion of the air flow from the zero-air generator can be diverted through the U-tube to flush the chemicals into the chamber. Gases injected in this manner are used to simulate atmospheric conditions. A mixing fan is mounted below these inputs on the inside the reactor,



which generally produces a well-mixed volume within 15 to 20 minutes after an injection.

185 For laboratory samples, BB aerosols are generated by combusting wood samples in a tube furnace. The  
furnace (Carbolite Gero, HST120300-120SN) holds an 85 mm OD, 80 mm ID, and 750 mm long quartz working  
tube and has a heated region of 300 mm. Stainless steel mounts and insulation plugs on either end enable the  
introduction and sampling of gasses. Air flow through the furnace is regulated by two mass flow controllers (MFC,  
Sierra Instruments), one each for clean air and nitrogen, with a combined flow rate of 10 L/min. In this way, the  
oxygen concentration available for combustion can be altered to study both oxygen-rich and oxygen-depleted  
190 environments. Clean air is supplied by house compressed air that passed through the zero-air generator, while  
nitrogen comes from a compressed cylinder (Airgas/National Welders, UN1066, industrial grade nitrogen). The  
furnace is preheated to 500 °C before the introduction of biomass samples. These samples are placed in a quartz  
combustion boat (AdValue Technology, FQ-BT-03), weighed and pushed into the center of the furnace with the aid  
of tongs, before replacing the input insulator and flange. The smoke and gasses produced from combustion are sent  
195 directly to the chamber via heated (200 °C), and ¼ inch OD stainless steel transfer tube. After introduction, they  
undergo cooling and dilution in a similar fashion to natural processes; as opposed to step-wise dilution and cooling,  
which introduces a hysteresis in the condensation of semi-volatile species.

## 2.5. Particle sampling and aerosol optical measurements

BB particles are taken from the FEP environmental chamber via graphite impregnated silicone tubing  
200 before entering a 710 µm impactor inlet (3.8 µm diameter cut point), neutralizer, and long differential mobility  
analyzer (DMA) (TSI, Model 3080), where the aerosol is size selected. Flow through the entire system (0.58  
sL/min) is produced by a pump within the condensation particle counter (CPC), and the DMA sheath flow is 2.8–6.0  
L/min in single blower mode. Aerosol flow then enters a ring-down cavity, where the aerosol extinction is measured  
over a range of wavelengths. The extinction coefficient  $\alpha_{ext}$  ( $m^{-1}$ ) is measured by the cavity ring-down system  
205 (CRDS), and the extinction cross section  $\sigma_{ext}$  ( $m^2$ /particle) is found using  $\alpha_{ext}$  and the number density of particles  
 $N_{CRD}$  (particles/cm<sup>3</sup>) in the cavity. After the CRDS, aerosol scattering coefficients are measured at 453, 554, and 698  
nm using the integrating nephelometer (TSI, model 3563), with particle concentration measured by the water-based  
condensation particle counter (WCPC, TSI, model 3788). Collectively, we have dubbed this system the Aerosol  
Optical Properties Measurement (AOPM) setup, and it has been extensively characterized (Singh et al., 2014). The  
210 absorption cross section is derived from the difference between the scattering and extinction cross sections. SSA is  
found by dividing the scattering by the extinction coefficient and adjusting for the relative number density in each  
instrument. Alternatively, the CPC can be attached directly after the DMA, where it is used to collect size  
distribution spectra of the biomass burning aerosol (i.e. as a scanning mobility particle sizer (SMPS)). SMPS spectra  
are corrected for multiple charging effects using built-in software algorithms. Additional sampling lines are used  
215 to measure ozone, nitric oxides, carbon monoxide, carbon dioxide, and hydrocarbons using the analyzers listed in  
Table 1. Measurements of NO, NO<sub>2</sub>, and O<sub>3</sub> are calibrated before and after a set of experiments, and those  
calibration factors are averaged to determine resulting concentrations. Figure 1 provides schematics of the chamber  
and the full experimental set up. Sampling lines are also used to collect particulates via impinger (AGI-4 type, Ace



220 Glass Inc., 7540-04 and 7542-10) and filters (Tisch Environmental, SF18040, 2- $\mu\text{m}$  pore). The impinger was  
initially developed to capture BB aerosol in situ, keeping the sample viable until it can be re-aerosolized in the  
laboratory (Singh et al., 2016). However, the size distribution of the impinged aerosol is different from fresh BB  
aerosol directly sampled from the chamber, as shown in Fig. 2. Additionally, recent work in our group has shown  
that retrieved refractive index values and the wavelength dependence of cross sections are altered by impinging and  
re-aerosolizing (Poudel et al., 2017). It is thought that most of the organic compounds are dissolved in the water and  
225 that particles were left leaving little to no coating when the samples are re-aerosolized. It has been shown that most  
of the BB aerosol material (on average about 50 %) is highly refractory organic material that is soluble in water  
(Mayol-Bracero et al., 2002), which leaves a nearly spherical compact core that produced a shift towards smaller  
mobility diameters in the size distribution. However, the size distribution of the impinged samples remains stable for  
an extended period, as shown in Fig. 2. Filter samples have been imaged by a scanning electron microscope (SEM)  
230 to determine their morphology for modeling refractive indices and optical properties using the T-matrix code  
(Poudel et al., 2017), and will be used in future studies to determine morphology of aged African BB particles.

### 3. Chamber characterization experiments, results, and discussion

The main limitation of chamber experiments is that particles and gas-phase species may be lost to chamber  
walls on timescales that are shorter than the timescales of the atmospheric processes being studied (Bian et al.,  
235 2015). Therefore, before use, chambers must be characterized to reduce uncertainties caused by the loss of gasses  
and particles in the chamber walls, as well as “background reactivity” which includes possibly surface chemistry  
which can generate gases, including reactive radical species (Carter et al., 2005; Weitkamp et al., 2007). Both  
particle-phase and vapor-phase wall losses must be considered in chamber experiments involving BB.

Typical chamber losses include dilution, vapor and particle deposition, gravitational settling, collisions with  
240 the walls of the chamber, agglomeration of smaller particles into larger ones, and leaks from the chamber (Crump  
and Seinfeld, 1981; Kamens et al., 1984). Particle loss rates are generally lower for larger chambers due to a smaller  
surface-area-to-volume ratio. Contamination was a large source of error in early experiments, leading to evacuable  
chamber designs. It is now common practice to condition chamber walls, especially FEP walls, by flushing the  
chamber with pure air and irradiating it to remove volatile particles (Akimoto et al., 1979; Grieshop et al., 2009).  
245 Off-gassing of  $\text{NO}_x$  and other contaminants can also increase uncertainty for low sample concentrations (Carter et  
al., 2005; Wang et al., 2014). Proper chamber evacuation or flushing is key to removing contaminants left behind  
after each experiment. Ozone, hydrogen peroxide, and nitrogen oxide are also sometimes used to react with these  
residual species in order to maintain chamber cleanliness (Babar et al., 2016).

The characterization experiments conducted for the NCAT chamber are described below and results are  
250 compared with similar chambers.

#### 3.1. Chamber mixing, flushing, and cleaning

A fan (12VDC spark free marine in-line electric blower (Shurflo, Yellow 3")) is used to thoroughly mix  
chamber injections with chamber air. The fan is rated to 3.40  $\text{m}^3/\text{min}$  and was used at 25–33 % of maximum power



255 by adjusting a variable voltage regulator. The injections of NO and NO<sub>2</sub>, were made using ~54 and 80 ppm,  
260 certified, of NO/NO<sub>2</sub> (Airgas/National Welders) respectively at 1 L/min for 20 min. Figure 3 shows four injections  
with 5 minute durations (for a total of 20 minutes of injection), spaced out every 20–30 minutes. Overall injection  
volume/concentration is the same for all experiments. They become well mixed after 15 minutes, as shown in Fig. 3.  
This includes the time it takes for particles to stabilize. The actual mixing time is nearly the same as the mixing time  
reported by other indoor chambers (Babar et al., 2016; Wang et al., 2014), which exhibit mixing times of 2–3  
minutes. Based on the available literature, the mixing time seems to be independent of the size of the chamber. The  
mixing fan rotation speed has been shown to provide better mixing but causes an increase in wall loss (Carter et al.,  
2005; Wang et al., 2011). Particles, however, do not become well mixed (i.e. have a relatively stable size  
distribution) until 60–90 minutes. This may be due in part to rapid agglomeration, coagulation, and particle growth.

265 After an experiment, the chamber is flushed with air from the zero-air generator at 30 L/min. An equal flow  
leaves the chamber through a gate valve and exhaust line that connects to the duct of the fume hood. While the vent  
line is equipped with a fan that is identical to the mixing fan, it is not typically used. At this rate, it usually takes less  
than 48 hours to remove all trace gases to reach acceptable zero values. Irradiation is not currently being used to  
clean the chamber since no contaminants are found after 48 hours. Particulates can take up to 72 hours to remove  
completely at the same flow rate. Particle removal was monitored using the DMA and the chamber was considered  
270 clean when particle concentrations were lower than the limit of detection; hence the longer time for particle removal  
from the chamber.

### 3.2. Wall loss rates of gases

Adsorption of gases on the chamber walls is the primary cause for the decrease of gas concentrations in the  
chamber. Wall loss rates of NO, NO<sub>2</sub>, and O<sub>3</sub> were evaluated by injecting  $0.12 \pm 0.01$  ppm of NO and  $0.18 \pm 0.01$  ppm  
275 of NO<sub>2</sub> during separate experiments and continuously monitoring their decay in the dark and near zero RH, as shown  
in Fig. 4. While the wall loss rate of O<sub>3</sub> was similarly calculated, the initial concentration of ozone injection is  
unknown due to the large volume of our chamber and the small amount of O<sub>3</sub> produced by the lamp (Spectroline,  
11SC-1) inside our ozone generator. Ozone injections took over three days to generate high enough concentrations  
in the chamber to measure the wall loss rate. It is likely that the injection rate was only slightly higher than the  
280 dilution rate. Wall loss rates are obtained by considering the wall loss as a first order process. To determine the total  
decay of a species in the gas phase, the natural log of its relative concentration is plotted over time, as shown in Eq.  
(1)

$$\text{Ln} \left( \frac{x(t)}{x(0)} \right) = -k_{\text{tot}} t \quad 1$$

285 where  $x(0)$  is the initial concentration of a species,  $x(t)$  is its concentration at a given time  $t$ , and  $k_{\text{tot}}$  is the total decay  
rate constant. When plotted this way,  $k_{\text{tot}}$  is the negative of the slope. The dilution rate constant,  $k_d$ , for each species  
can be determined by summing the sampling flow rates  $f$  for the chamber and dividing them by the chamber volume  
 $V$ :



$$k_d = \frac{\sum_i (f_i)}{V} \quad 2$$

290 Since this factor is independent of concentration, it can be used for all species. It is then subtracted from  $k_{tot}$  to get the wall loss rate,  $k_{wl}$ , for the species:

$$k_{wl} = k_{tot} - k_d \quad 3$$

295 This factor includes losses due to gravitational settling, impaction with the walls, and leaks from the chamber. For the NCAT chamber loss rate constants for NO, NO<sub>2</sub>, and O<sub>3</sub> are  $(7.40 \pm 0.01) \times 10^{-4}$ ,  $(3.47 \pm 0.01) \times 10^{-4}$ , and  $(5.90 \pm 0.08) \times 10^{-4} \text{ min}^{-1}$ , respectively. Table 2 shows comparisons with similar chambers which represents averages of several measurements. The errors are one standard deviation (1s) of these repeat measurements. Minimizing surface area to volume ratios, and attempting to isolate the sampled flow from the walls help reduce losses, but challenges remain (Bruns et al., 2015). However, our results are slightly faster than chambers with lower surface area to volume ratios. A possible reason for this is that gas transfer towards the walls are driven by the turbulence inside the chamber (La et al., 2016), which is a result of fan position and speed. Since, fan speeds were not provided for all chambers, wall loss comparisons become difficult.

### 3.3. Particle wall loss rate and shift in size distribution

305 Biomass burning particles produced in a tube furnace were introduced into the chamber as described in section 2.4. To enable the comparison with other chambers, white pine wood was chosen. It was weighed to ~100 mg and placed in a quartz combustion boat which was in turn placed at the center of the furnace. After the initial combustion of biomass, multiple peaks are seen in the size distribution of the resulting BB aerosol. Both the number of peaks and the diameters they correspond to shift apparently at random as the particles are being mixed inside the chamber. After ~60–90 minutes, the size distribution resolves into a single log-normal distribution with a peak particle mobility diameter near 246 nm for pine. The total particle concentration was  $\sim 1.5 \times 10^5 \text{ particles}\cdot\text{cm}^{-3}$  after mixing. Even under dark conditions (i.e. the UV lamps are off and near zero RH), this distribution continues to shift towards larger particle sizes, reaching peak mobility diameters of ~340 nm after 7.5 hours. This changing distribution can be seen in Fig. 5.

310 As with the gas wall loss rates, particle wall loss, or deposition, follows the same first-order process, and is dependent on the concentration and particle size. It is given by Eq. (4) (Cocker et al., 2001):

$$315 \quad \text{Ln} \left( \frac{N(D_p, t)}{N(D_p, 0)} \right) = -k_{dep}(D_p)t \quad 4$$

where  $N(D_p, t)$  is the number concentration in  $\text{particles}\cdot\text{cm}^{-3}$  with diameter  $D_p$ , and  $k_{dep}(D_p)$  is the wall loss rate constant of particle with diameter  $D_p$ . While the rate constant varied over time, it was consistent during the beginning, middle and end of the experiment. For particle diameters of 100 nm, a rate constant of  $(2.46 \pm 0.11) \times$



320  $10^{-3} \text{ min}^{-1}$  was found once the size distribution stabilized after  $\sim 7.5$  hours. The particle wall loss rates decreased  
with increasing particle diameter suggesting smaller particles deposit faster (Wang et al., 2014; Takekawa et al.,  
2003). For  $D_p = 100 \text{ nm}$  the particle wall loss rate for NCAT chamber is comparable to other chambers reported for  
example  $3.83 \times 10^{-3} \text{ min}^{-1}$  for the Guangzhou ( $30 \text{ m}^3$ ) chamber (Wang et al., 2014) and  $3.96 \times 10^{-3} \text{ min}^{-1}$  for the  $7$   
 $\text{m}^3$  KNU chamber (Babar et al., 2016). A smaller value of  $7.5 \times 10^{-4} \text{ min}^{-1}$  was reported for the  $29 \text{ m}^3$  Ilmari  
325 chamber (Leskinen et al., 2015). This is much lower than most reported particle wall losses. There were no mixing  
fans in the Ilmari chamber, which was used to explain the difference. Mixing fans can enhance wall deposition by  
increasing turbulence inside the chamber. The wall loss rate was faster initially and leveled off after 10 hours in the  
NCAT chamber. Similar observations were reported in the Ilmari chamber (Leskinen et al., 2015).

It is likely that the size distribution changes due to a competition between wall loss and particle  
coagulation, with subsequent formation of larger particles. When modeled as a second order process, a poor  
330 relationship between  $1/N(100 \text{ nm}, t)$  and  $t$  was found. However, for polydisperse aerosol number loss (i.e. when the  
total particle volume concentration ( $\text{nm}^3 \cdot \text{cm}^{-3}$ ) was plotted), a good fit was found for a first order decay. The loss  
rate constant for this process was  $(1.34 \pm 0.02) \times 10^{-3} \text{ min}^{-1}$  which corresponds to a life time of 12.4 hours. If one  
assumes that particle volume is conserved (i.e. that condensation or evaporation of semivolatile species is either very  
fast or absent), a better fit would be expected. These results are comparable to other chambers, which were  $2.8 \times$   
335  $10^{-3} \text{ min}^{-1}$  for the Guangzhou chamber (Wang et al., 2014)  $3.48 \times 10^{-3} \text{ min}^{-1}$  for Paul Scherrer Institute, (Paulsen et  
al., 2005) and  $1.5 \times 10^{-3} \text{ min}^{-1}$  for the California Institute of Technology Chamber (Cocker et al., 2001). More  
experiments are planned to understand the relationship between initial particle number concentration and the loss  
rate.

Recent experiments have demonstrated that POA from biomass burning contains semi-volatile compounds,  
340 which can evaporate during dilution (May et al., 2013). Particle wall losses have been used to quantitatively correct  
observed aerosol concentrations to deduce SOA formation in smog chambers (Hennigan et al., 2011) by assuming  
that semi-volatile compounds are in equilibrium with the particles deposited in the walls instead of the walls  
themselves. The magnitude of vapor wall loss has not been considered in most smog chamber studies, since the  
values are not constrained (Bian et al., 2015). Recently, Zhang et al. (2014) showed that the vapor wall loss can  
345 underestimate SOA formation. It is therefore necessary to consider vapor wall loss when introducing BB smoke in  
chambers. We did not consider vapor wall loss in this work since the focus was on POA.

Particle and vapor losses to the walls of a smog chamber during an experiment can alter the composition of  
the smoke being studied, causing great uncertainty for quantifying SOA production (Weitkamp et al., 2007). In one  
study with cigarette smoke, particle deposition to chamber walls ranged from 23 % to 78 %, which is dependent on  
350 the wall material and independent of particle concentration and flow rate (Schick et al., 2012). Other studies  
simulated the chamber wall loss of particles and vapors from BB smoke (Bian et al., 2015; Trump et al., 2016). Bain  
et al. found that 41 % of the initial particle-phase organic mass was lost during the experiments, with 65 % of this  
loss from direct particle deposition and the remaining 35 % from evaporation of OA and subsequent loss of vapor to  
the walls. The later mechanism is influenced by dilution during the introduction of particles into the chamber. The  
355 shift in the size distribution to larger mobility diameters can also be explained by smaller particles diffusing towards



the chamber walls more quickly and coagulating more rapidly, as was observed by Wang et al. (2014) and Takekawa et al. (2003).

Particle loss rates were also studied in detail by Pierce et al. (2008). Experiments involving wood combustion generally produce BB aerosols in the range of 70–230 nm in mobility diameter, with most of the particles having a mobility diameter of less than 500 nm (Kamens et al., 1984). This shift can be lessened by using total particle concentrations of less than 25,000 particles·cm<sup>-3</sup> (McMurry and Grosjean, 1985). We plan to study size distribution of photochemically aged BB aerosol in greater detail as part of our ongoing research goals.

### 3.4. Light intensity and temperature

The UV lamps (Sylvania, F30T8/350BL/ECO, 36") used for the NCAT chamber simulate the UV portion of the solar spectrum, as shown in Fig. 6. For this range, the FEP film is over 90 % transparent (DuPont, 2010). Average light intensity for the chamber is modeled using the photolysis rate of NO<sub>2</sub>, which is estimated by a steady-state actinometry (Wang et al., 2014). The photolysis rate constant  $j_{NO_2}$  is calculated from the measured concentrations of NO, NO<sub>2</sub>, and O<sub>3</sub> after the lights are turned on and the reaction reached equilibrium, and is given by Eq. (5)

370

$$j_{NO_2} = \frac{k_{NO+O_3} [O_3] [NO]}{[NO_2]} \quad 5$$

where [NO], [O<sub>3</sub>], and [NO<sub>2</sub>] represent concentrations (molecule·cm<sup>-3</sup>), and  $k_{NO+O_3}$  is the rate constant of NO<sub>2</sub> formation from ozone and NO, which is  $k_{NO+O_3} = 1.9 \times 10^{-14} \text{ cm}^3 \cdot \text{mol}^{-1} \cdot \text{sec}^{-1}$  (Burkholder, 2015). The average photolysis rate constant for our chamber is  $0.165 \pm 0.005 \text{ min}^{-1}$  at full light intensity, as shown in Fig. 7. The maximum NO<sub>2</sub> photolysis rate in our chamber is comparable to those reported in other indoor chambers, such as 0.132 min<sup>-1</sup> in the 29 m<sup>3</sup> Ilmari chamber (Leskinen et al., 2015); 0.12 min<sup>-1</sup> in the 27 m<sup>3</sup> chamber at the Paul Scherrer Institute (Paulsen et al., 2005); 0.19 min<sup>-1</sup> in the 90 m<sup>3</sup> environmental chamber at the University of California, Riverside (Carter et al., 2005); 1.5 min<sup>-1</sup> in the 28 m<sup>3</sup> chamber at the California Institute of Technology (Cocker et al., 2001); and comparable to most recent chambers provided in Table 2. When only half of the lights were powered, values of  $0.091 \pm 0.005 \text{ min}^{-1}$  and  $0.0846 \pm 0.0042 \text{ min}^{-1}$  were obtained for the door side and window side, respectively. The lower rate constant for the window side may be due to the observation windows built into the chamber, which are located near the window side and may allow light to escape.

The effect of excluding the rate of NO<sub>2</sub> removal on  $j_{NO_2}$  was also examined. Since the rate constant for the total loss of NO<sub>2</sub> is relatively small ( $4.06 \times 10^{-4} \text{ min}^{-1}$ ),  $j_{NO_2}$  only decreased by 0.24–0.30 % when this factor was included. As such, while this is not significant for the NCAT chamber, it should be considered for chambers with lower light intensity or when a chamber is sampled at flow rates that are high relative to the chamber volume.

The actinic flux of the chamber was also measured (Hamilton et al., 2011). The spectrum of the UV lamps, the measured  $j$  value for NO<sub>2</sub> under several conditions, and the quantum yield and absorption cross section for NO<sub>2</sub> (Burkholder, 2015) were used to determine the actinic flux in the region where these lights would be



390 photochemically active towards NO<sub>2</sub>, which is 296–424 nm. In this method, the spectrum was integrated using the  
trapezoidal method and normalized to 1 photons•nm<sup>-2</sup>•s<sup>-1</sup> over the 296–424 nm range. When both banks are  
engaged, a flux of  $(7.42 \pm 0.24) \times 10^{17}$  photons•nm•cm<sup>-2</sup>•s<sup>-1</sup> was found over this wavelength range. When taken  
over the entire range of the spectrometer (296.0–516.8 nm, the flux becomes  $(7.96 \pm 0.25) \times 10^{17}$   
395 photons•nm•cm<sup>-2</sup>•s<sup>-1</sup>. The flux for the bank of lights near the door was  $(4.22 \pm 0.24) \times 10^{17}$  and  $(4.52 \pm 0.26) \times 10^{17}$   
photons•nm•cm<sup>-2</sup>•s<sup>-1</sup> over 296–424 nm and 296.0–516.8 nm, respectively. Similarly, the set near the windows were  
 $(3.92 \pm 0.18) \times 10^{17}$  and  $(4.20 \pm 0.20) \times 10^{17}$  photons•nm•cm<sup>-2</sup>•s<sup>-1</sup> for their respective ranges.

Indoor smog chambers present a potential fire hazard due to the heat generated by the UV lamps and  
trapped inside the reflective walls of the chamber. With the lamps on, the maximum temperature recorded in the  
NCAT chamber was under 30 °C after 5 hours of use, as shown in Fig. 8. The typical change in temperature is less  
400 than 10 °C after 5 hours, with most of the increase occurring in the first hour of operation.

### 3.5. Soot generation and characterization

Most laboratory studies using smog chambers utilize large combustion chambers (Bian et al., 2015) or  
residential wood stoves (Grieshop et al., 2009) to generate BB aerosols from combustion. Others use hoods to  
sample smoke in a more ambient environment (Singh et al., 2016). While these methods are useful in determining  
405 the broader impact of BB, they possess too many poorly constrained variables. Even when a single fuel type is used,  
there remain contaminants in the surrounding air. Additionally, different parts of the same fire may be undergoing  
different burning stages, which have distinctly different combustion profiles. To avoid these issues, we have  
employed a tube furnace, described in greater detail in section 2.4, which allows us to combust a measured amount  
of biomass at a specific temperature to more accurately investigate variations in burning stages. In addition to  
410 temperature control, this design also allows us to vary the oxygen available for combustion, to investigate smoke  
produced from oxygen-starved burns. This control over the combustion process will allow us to accurately measure  
the contribution of specific species (sources) to the aerosol mass loading of the environment.

Most indirect (and some direct) aerosol optical measurement techniques involve collecting the samples on  
filters before they can be analyzed. However, the use of filters can affect these measurements due to multiple  
415 scattering by the filter itself, the spatial distribution of the particles on the filter, and changes in the morphology of  
these particles upon deposition (Bond and Bergstrom, 2006; Moosmüller et al., 2009). Further, samples collected on  
filters are more prone to artifacts due to their highly-concentrated nature (Moosmüller et al., 2009). Direct  
measurements can be taken using a combination of techniques that maintain the state of the aerosol, such as one of  
the following methods: photoacoustic spectroscopy (PAS) and integrating nephelometry to measure absorption and  
420 scattering, respectively, with extinction being the sum of the two; or CRDS and integrating nephelometry to measure  
extinction and scattering, respectively, while absorption is determined from extinction minus scattering. We use the  
extinction-minus-scattering method in our lab. For highly absorbing particles, such as BC, this method is quite  
reasonable (Bond and Bergstrom, 2006), as it has been shown elsewhere (Lewis et al., 2009; Langridge et al., 2013)  
that PAS can include large errors under certain conditions. Additionally, our CRDS uses tunable lasers that provide  
425 a wide range of solar wavelengths (Singh et al., 2016), while most studies are limited to a single or a few specific



wavelengths. The setup in our laboratory will allow us to sample particles directly from the chamber, and measure their size distributions and optical properties as a function of aerosol age.

#### 4. Conclusion

430 We have shown here that the new NCAT indoor smog chamber can simulate atmospheric conditions for  
studying radiative impacts of BB aerosols. The chamber demonstrated gas and particle loss rates, and other  
properties comparable to similar indoor smog chambers. Novel aspects of this chamber include the use of a tube  
furnace and the combustion of small quantities of fuel under controlled conditions of temperature and gas (nitrogen  
and air) flow, which enables the simulation of different burning stages and measuring of the combined combustion  
efficiency of each burning stage in a controlled manner. The chamber is connected to a SMPS to determine the size  
435 distributions of fresh and aged BB aerosols as they form and change in size over time. BB particles are sampled  
directly into a cavity ring-down spectrometer and a nephelometer for measuring their scattering and extinction cross  
sections using tunable lasers that provides a wider range of optical wavelengths than previously reported. This  
characterized and calibrated system will determine the effects of fuel type, aging, and humidity on the size  
distribution, optical properties, and physicochemical properties of biomass burning aerosols native to sub-Saharan  
440 Africa for the first time.

#### 5. Acknowledgements

The authors acknowledge Marquin Spann for his experimental assistance and the financial support provided by the National Science Foundation under grant # NSF-AGS 1555479 to accomplish this work.



## References

- Abel, S. J., Haywood, J. M., Highwood, E. J., Li, J., and Buseck, P. R.: Evolution of biomass burning aerosol properties from an agricultural fire in southern Africa, *Geophysical Research Letters*, 30, 1783, 10.1029/2003GL017342, 2003.
- Akimoto, H., Hoshino, M., Inoue, G., Sakamaki, F., Washida, N., and Okuda, M.: Design and characterization of the evacuable and bakable photochemical smog chamber, *Environmental Science & Technology*, 13, 471-475, 10.1021/es60152a014, 1979.
- Andreae, M. O., Andreae, T. W., Annegarn, H., Beer, J., Cachier, H., Le Canut, P., Elbert, W., Maenhaut, W., Salma, I., Wienhold, F. G., and Zenker, T.: Airborne studies of aerosol emissions from savanna fires in southern Africa: 2. Aerosol chemical composition, *Journal of Geophysical Research: Atmospheres*, 103, 32119-32128, 10.1029/98JD02280, 1998.
- Andreae, M. O., and Merlet, P.: Emission of trace gases and aerosols from biomass burning, *Global Biogeochemical Cycles*, 15, 955-966, 10.1029/2000GB001382, 2001.
- Babar, Z. B., Park, J.-H., Kang, J., and Lim, H.-J.: Characterization of a Smog Chamber for Studying Formation and Physicochemical Properties of Secondary Organic Aerosol, *Aerosol and Air Quality Research*, 16, 3102-3113, 10.4209/aaqr.2015.10.0580, 2016.
- Bian, Q., May, A. A., Kreidenweis, S. M., and Pierce, J. R.: Investigation of particle and vapor wall-loss effects on controlled wood-smoke smog-chamber experiments, *Atmos. Chem. Phys.*, 15, 11027-11045, 10.5194/acp-15-11027-2015, 2015.
- Bond, T. C., and Bergstrom, R. W.: Light Absorption by Carbonaceous Particles: An Investigative Review, *Aerosol Science and Technology*, 40, 27-67, 10.1080/02786820500421521, 2006.
- Bond, T. C., Doherty, S. J., Fahey, D. W., Forster, P. M., Berntsen, T., DeAngelo, B. J., Flanner, M. G., Ghan, S., Kärcher, B., Koch, D., Kinne, S., Kondo, Y., Quinn, P. K., Sarofim, M. C., Schultz, M. G., Schulz, M., Venkataraman, C., Zhang, H., Zhang, S., Bellouin, N., Guttikunda, S. K., Hopke, P. K., Jacobson, M. Z., Kaiser, J. W., Klimont, Z., Lohmann, U., Schwarz, J. P., Shindell, D., Storelvmo, T., Warren, S. G., and Zender, C. S.: Bounding the role of black carbon in the climate system: A scientific assessment, *Journal of Geophysical Research: Atmospheres*, 118, 5380-5552, 10.1002/jgrd.50171, 2013.
- Bruns, E. A., El Haddad, I., Keller, A., Klein, F., Kumar, N. K., Pieber, S. M., Corbin, J. C., Slowik, J. G., Brune, W. H., Baltensperger, U., and Prévôt, A. S. H.: Inter-comparison of laboratory smog chamber and flow reactor systems on organic aerosol yield and composition, *Atmos. Meas. Tech.*, 8, 2315-2332, 10.5194/amt-8-2315-2015, 2015.
- Burkholder, J. B., Sander, S.P., Abbatt, J., Barker, J.R., Huie, R. E., Kolb, C. E., Kurylo, M. J., Orkin, V. L., Wilmouth, D. M., Wine, P. H.: Chemical Kinetics and Photochemical Data for Use in Atmospheric Studies, Evaluation No. 18, Jet Propulsion Laboratory, Pasadena, 2015.
- Carter, W. P. L., Cocker, D. R., Fitz, D. R., Malkina, I. L., Bumiller, K., Sauer, C. G., Pisano, J. T., Bufalino, C., and Song, C.: A new environmental chamber for evaluation of gas-phase chemical mechanisms and secondary aerosol formation, *Atmospheric Environment*, 39, 7768-7788, <https://doi.org/10.1016/j.atmosenv.2005.08.040>, 2005.
- Cocker, D. R., Flagan, R. C., and Seinfeld, J. H.: State-of-the-Art Chamber Facility for Studying Atmospheric Aerosol Chemistry, *Environmental Science & Technology*, 35, 2594-2601, 10.1021/es0019169, 2001.
- Crump, J. G., and Seinfeld, J. H.: Turbulent deposition and gravitational sedimentation of an aerosol in a vessel of arbitrary shape, *Journal of Aerosol Science*, 12, 405-415, [https://doi.org/10.1016/0021-8502\(81\)90036-7](https://doi.org/10.1016/0021-8502(81)90036-7), 1981.



De Gouw, J., and Jimenez, J. L.: Organic Aerosols in the Earth's Atmosphere, *Environmental Science & Technology*, 43, 7614-7618, 10.1021/es9006004, 2009.

DuPont FEP Film Fluorocarbon Film Information Bulletin, access: December 21, 2010.

Engelhart, G. J., Hennigan, C. J., Miracolo, M. A., Robinson, A. L., and Pandis, S. N.: Cloud condensation nuclei activity of fresh primary and aged biomass burning aerosol, *Atmos. Chem. Phys.*, 12, 7285-7293, 10.5194/acp-12-7285-2012, 2012.

Formenti, P., Elbert, W., Maenhaut, W., Haywood, J., Osborne, S., and Andreae, M. O.: Inorganic and carbonaceous aerosols during the Southern African Regional Science Initiative (SAFARI 2000) experiment: Chemical characteristics, physical properties, and emission data for smoke from African biomass burning, *Journal of Geophysical Research: Atmospheres*, 108, 8488, 10.1029/2002JD002408, 2003.

Gentner, D. R., Isaacman, G., Worton, D. R., Chan, A. W. H., Dallmann, T. R., Davis, L., Liu, S., Day, D. A., Russell, L. M., Wilson, K. R., Weber, R., Guha, A., Harley, R. A., and Goldstein, A. H.: Elucidating secondary organic aerosol from diesel and gasoline vehicles through detailed characterization of organic carbon emissions, *Proceedings of the National Academy of Sciences*, 109, 18318-18323, 10.1073/pnas.1212272109, 2012.

Gentner, D. R., Jathar, S. H., Gordon, T. D., Bahreini, R., Day, D. A., El Haddad, I., Hayes, P. L., Pieber, S. M., Platt, S. M., de Gouw, J., Goldstein, A. H., Harley, R. A., Jimenez, J. L., Prévôt, A. S. H., and Robinson, A. L.: Review of Urban Secondary Organic Aerosol Formation from Gasoline and Diesel Motor Vehicle Emissions, *Environmental Science & Technology*, 51, 1074-1093, 10.1021/acs.est.6b04509, 2017.

Giordano, M. R., and Asa-Awuku, A.: Rebuttal to Correspondence on "Changes in Droplet Surface Tension Affect the Observed Hygroscopicity of Photochemically Aged Biomass Burning Aerosol", *Environmental Science & Technology*, 48, 2084-2085, 10.1021/es405374r, 2014.

Grieshop, A. P., Logue, J. M., Donahue, N. M., and Robinson, A. L.: Laboratory investigation of photochemical oxidation of organic aerosol from wood fires 1: measurement and simulation of organic aerosol evolution, *Atmos. Chem. Phys.*, 9, 1263-1277, 10.5194/acp-9-1263-2009, 2009.

Hallquist, M., Wenger, J. C., Baltensperger, U., Rudich, Y., Simpson, D., Claeys, M., Dommen, J., Donahue, N. M., George, C., Goldstein, A. H., Hamilton, J. F., Herrmann, H., Hoffmann, T., Iinuma, Y., Jang, M., Jenkin, M. E., Jimenez, J. L., Kiendler-Scharr, A., Maenhaut, W., McFiggans, G., Mentel, T. F., Monod, A., Prévôt, A. S. H., Seinfeld, J. H., Surratt, J. D., Szmigielski, R., and Wildt, J.: The formation, properties and impact of secondary organic aerosol: current and emerging issues, *Atmos. Chem. Phys.*, 9, 5155-5236, 10.5194/acp-9-5155-2009, 2009.

Hamilton, J. F., Rami Alfarra, M., Wyche, K. P., Ward, M. W., Lewis, A. C., McFiggans, G. B., Good, N., Monks, P. S., Carr, T., White, I. R., and Purvis, R. M.: Investigating the use of secondary organic aerosol as seed particles in simulation chamber experiments, *Atmos. Chem. Phys.*, 11, 5917-5929, 10.5194/acp-11-5917-2011, 2011.

Harvey, R. M., Bateman, A. P., Jain, S., Li, Y. J., Martin, S., and Petrucci, G. A.: Optical Properties of Secondary Organic Aerosol from cis-3-Hexenol and cis-3-Hexenyl Acetate: Effect of Chemical Composition, Humidity, and Phase, *Environmental Science & Technology*, 50, 4997-5006, 10.1021/acs.est.6b00625, 2016.

Hawkins, L. N., and Russell, L. M.: Oxidation of ketone groups in transported biomass burning aerosol from the 2008 Northern California Lightning Series fires, *Atmospheric Environment*, 44, 4142-4154, <https://doi.org/10.1016/j.atmosenv.2010.07.036>, 2010.

Hennigan, C. J., Miracolo, M. A., Engelhart, G. J., May, A. A., Presto, A. A., Lee, T., Sullivan, A. P., McMeeking, G. R., Coe, H., Wold, C. E., Hao, W. M., Gilman, J. B., Kuster, W. C., de Gouw, J., Schichtel, B. A., Collett Jr, J. L., Kreidenweis, S. M., and Robinson, A. L.: Chemical and physical transformations of organic aerosol from the photo-oxidation of open biomass burning emissions in an environmental chamber, *Atmos. Chem. Phys.*, 11, 7669-7686, 10.5194/acp-11-7669-2011, 2011.



Hodzic, A., Madronich, S., Bohn, B., Massie, S., Menut, L., and Wiedinmyer, C.: Wildfire particulate matter in Europe during summer 2003: meso-scale modeling of smoke emissions, transport and radiative effects, *Atmos. Chem. Phys.*, 7, 4043-4064, 10.5194/acp-7-4043-2007, 2007.

Ichoku, C., Giglio, L., Wooster, M. J., and Remer, L. A.: Global characterization of biomass-burning patterns using satellite measurements of fire radiative energy, *Remote Sensing of Environment*, 112, 2950-2962, <https://doi.org/10.1016/j.rse.2008.02.009>, 2008.

IPCC: Climate Change 2013: The Physical Science Basis. Contribution of Working Group I to the Fifth Assessment Report of the Intergovernmental Panel on Climate Change, Cambridge, United Kingdom 1535, 2013.

Jimenez, J. L., Canagaratna, M. R., Donahue, N. M., Prevot, A. S. H., Zhang, Q., Kroll, J. H., DeCarlo, P. F., Allan, J. D., Coe, H., Ng, N. L., Aiken, A. C., Docherty, K. S., Ulbrich, I. M., Grieshop, A. P., Robinson, A. L., Duplissy, J., Smith, J. D., Wilson, K. R., Lanz, V. A., Hueglin, C., Sun, Y. L., Tian, J., Laaksonen, A., Raatikainen, T., Rautiainen, J., Vaattovaara, P., Ehn, M., Kulmala, M., Tomlinson, J. M., Collins, D. R., Cubison, M. J., Dunlea, J., Huffman, J. A., Onasch, T. B., Alfarra, M. R., Williams, P. I., Bower, K., Kondo, Y., Schneider, J., Drewnick, F., Borrmann, S., Weimer, S., Demerjian, K., Salcedo, D., Cottrell, L., Griffin, R., Takami, A., Miyoshi, T., Hatakeyama, S., Shimojo, A., Sun, J. Y., Zhang, Y. M., Dzepina, K., Kimmel, J. R., Sueper, D., Jayne, J. T., Herndon, S. C., Trimborn, A. M., Williams, L. R., Wood, E. C., Middlebrook, A. M., Kolb, C. E., Baltensperger, U., and Worsnop, D. R.: Evolution of Organic Aerosols in the Atmosphere, *Science*, 326, 1525-1529, 10.1126/science.1180353, 2009.

Kamens, R. M., Rives, G. D., Perry, J. M., Bell, D. A., Paylo, R. F., Goodman, R. G., and Claxton, L. D.: Mutagenic changes in dilute wood smoke as it ages and reacts with ozone and nitrogen dioxide. An outdoor chamber study, *Environmental Science & Technology*, 18, 523-530, 10.1021/es00125a008, 1984.

Kanakidou, M., Seinfeld, J. H., Pandis, S. N., Barnes, I., Dentener, F. J., Facchini, M. C., Van Dingenen, R., Ervens, B., Nenes, A., Nielsen, C. J., Swietlicki, E., Putaud, J. P., Balkanski, Y., Fuzzi, S., Horth, J., Moortgat, G. K., Winterhalter, R., Myhre, C. E. L., Tsigaridis, K., Vignati, E., Stephanou, E. G., and Wilson, J.: Organic aerosol and global climate modelling: a review, *Atmos. Chem. Phys.*, 5, 1053-1123, 10.5194/acp-5-1053-2005, 2005.

Kim, H., and Paulson, S. E.: Real refractive indices and volatility of secondary organic aerosol generated from photooxidation and ozonolysis of limonene,  $\alpha$ -pinene and toluene, *Atmos. Chem. Phys.*, 13, 7711-7723, 10.5194/acp-13-7711-2013, 2013.

Koch, D., Menon, S., Genio, A. D., Ruedy, R., Alienov, I., and Schmidt, G. A.: Distinguishing Aerosol Impacts on Climate over the Past Century, *Journal of Climate*, 22, 2659-2677, 10.1175/2008jcli2573.1, 2009.

La, Y. S., Camredon, M., Ziemann, P. J., Valorso, R., Matsunaga, A., Lannuque, V., Lee-Taylor, J., Hodzic, A., Madronich, S., and Aumont, B.: Impact of chamber wall loss of gaseous organic compounds on secondary organic aerosol formation: explicit modeling of SOA formation from alkane and alkene oxidation, *Atmos. Chem. Phys.*, 16, 1417-1431, 10.5194/acp-16-1417-2016, 2016.

Lamarque, J. F., Bond, T. C., Eyring, V., Granier, C., Heil, A., Klimont, Z., Lee, D., Liousse, C., Mieville, A., Owen, B., Schultz, M. G., Shindell, D., Smith, S. J., Stehfest, E., Van Aardenne, J., Cooper, O. R., Kainuma, M., Mahowald, N., McConnell, J. R., Naik, V., Riahi, K., and van Vuuren, D. P.: Historical (1850–2000) gridded anthropogenic and biomass burning emissions of reactive gases and aerosols: methodology and application, *Atmos. Chem. Phys.*, 10, 7017-7039, 10.5194/acp-10-7017-2010, 2010.

Langridge, J. M., Richardson, M. S., Lack, D. A., Brock, C. A., and Murphy, D. M.: Limitations of the Photoacoustic Technique for Aerosol Absorption Measurement at High Relative Humidity, *Aerosol Science and Technology*, 47, 1163-1173, 10.1080/02786826.2013.827324, 2013.

Leskinen, A., Yli-Pirilä, P., Kuuspallo, K., Sippula, O., Jalava, P., Hirvonen, M. R., Jokiniemi, J., Virtanen, A., Komppula, M., and Lehtinen, K. E. J.: Characterization and testing of a new environmental chamber, *Atmos. Meas. Tech.*, 8, 2267-2278, 10.5194/amt-8-2267-2015, 2015.



Levin, E. J. T., McMeeking, G. R., Carrico, C. M., Mack, L. E., Kreidenweis, S. M., Wold, C. E., Moosmüller, H., Arnott, W. P., Hao, W. M., Collett, J. L., and Malm, W. C.: Biomass burning smoke aerosol properties measured during Fire Laboratory at Missoula Experiments (FLAME), *Journal of Geophysical Research: Atmospheres*, 115, D18210, 10.1029/2009JD013601, 2010.

Lewis, K. A., Arnott, W. P., Moosmüller, H., Chakrabarty, R. K., Carrico, C. M., Kreidenweis, S. M., Day, D. E., Malm, W. C., Laskin, A., Jimenez, J. L., Ulbrich, I. M., Huffman, J. A., Onasch, T. B., Trimborn, A., Liu, L., and Mishchenko, M. I.: Reduction in biomass burning aerosol light absorption upon humidification: roles of inorganically-induced hygroscopicity, particle collapse, and photoacoustic heat and mass transfer, *Atmos. Chem. Phys.*, 9, 8949-8966, 10.5194/acp-9-8949-2009, 2009.

Li, C., Ma, Z., Chen, J., Wang, X., Ye, X., Wang, L., Yang, X., Kan, H., Donaldson, D. J., and Mellouki, A.: Evolution of biomass burning smoke particles in the dark, *Atmospheric Environment*, 120, 244-252, <https://doi.org/10.1016/j.atmosenv.2015.09.003>, 2015.

Liousse, C., Guillaume, B., Grégoire, J. M., Mallet, M., Galy, C., Pont, V., Akpo, A., Bedou, M., Castéra, P., Dungall, L., Gardrat, E., Granier, C., Konaré, A., Malavelle, F., Mariscal, A., Mieville, A., Rosset, R., Serça, D., Solmon, F., Tummon, F., Assamoi, E., Yoboué, V., and Van Velthoven, P.: Updated African biomass burning emission inventories in the framework of the AMMA-IDAF program, with an evaluation of combustion aerosols, *Atmos. Chem. Phys.*, 10, 9631-9646, 10.5194/acp-10-9631-2010, 2010.

Liu, S., Aiken, A. C., Arata, C., Dubey, M. K., Stockwell, C. E., Yokelson, R. J., Stone, E. A., Jayarathne, T., Robinson, A. L., DeMott, P. J., and Kreidenweis, S. M.: Aerosol single scattering albedo dependence on biomass combustion efficiency: Laboratory and field studies, *Geophysical Research Letters*, 41, 742-748, 10.1002/2013GL058392, 2014.

Mack, L. A., Levin, E. J. T., Kreidenweis, S. M., Obrist, D., Moosmüller, H., Lewis, K. A., Arnott, W. P., McMeeking, G. R., Sullivan, A. P., Wold, C. E., Hao, W. M., Collett Jr, J. L., and Malm, W. C.: Optical closure experiments for biomass smoke aerosols, *Atmos. Chem. Phys.*, 10, 9017-9026, 10.5194/acp-10-9017-2010, 2010.

Mack, L. E.: Cavity Ring-Down Spectroscopy and the Retrieval of Aerosol Optical Properties from Biomass Burning During Flame 2, Master's, Colorado State University, CO, USA, 2008.

May, A. A., Levin, E. J. T., Hennigan, C. J., Riipinen, I., Lee, T., Collett, J. L., Jimenez, J. L., Kreidenweis, S. M., and Robinson, A. L.: Gas-particle partitioning of primary organic aerosol emissions: 3. Biomass burning, *Journal of Geophysical Research: Atmospheres*, 118, 2013JD020286, 10.1002/jgrd.50828, 2013.

Mayol-Bracero, O. L., Guyon, P., Graham, B., Roberts, G., Andreae, M. O., Decesari, S., Facchini, M. C., Fuzzi, S., and Artaxo, P.: Water-soluble organic compounds in biomass burning aerosols over Amazonia 2. Apportionment of the chemical composition and importance of the polyacidic fraction, *Journal of Geophysical Research: Atmospheres*, 107, LBA 59-51-LBA 59-15, 10.1029/2001JD000522, 2002.

McMeeking, G. R., Kreidenweis, S. M., Baker, S., Carrico, C. M., Chow, J. C., Collett, J. L., Hao, W. M., Holden, A. S., Kirchstetter, T. W., Malm, W. C., Moosmüller, H., Sullivan, A. P., and Wold, C. E.: Emissions of trace gases and aerosols during the open combustion of biomass in the laboratory, *Journal of Geophysical Research: Atmospheres*, 114, D19210, 10.1029/2009JD011836, 2009.

McMurry, P. H., and Grosjean, D.: Gas and aerosol wall losses in Teflon film smog chambers, *Environmental Science & Technology*, 19, 1176-1182, 10.1021/es00142a006, 1985.

Moosmüller, H., Chakrabarty, R. K., and Arnott, W. P.: Aerosol light absorption and its measurement: A review, *Journal of Quantitative Spectroscopy and Radiative Transfer*, 110, 844-878, <https://doi.org/10.1016/j.jqsrt.2009.02.035>, 2009.



Murphy, D. M., Cziczo, D. J., Froyd, K. D., Hudson, P. K., Matthew, B. M., Middlebrook, A. M., Peltier, R. E., Sullivan, A., Thomson, D. S., and Weber, R. J.: Single-particle mass spectrometry of tropospheric aerosol particles, *Journal of Geophysical Research: Atmospheres*, 111, D23832, [10.1029/2006JD007340](https://doi.org/10.1029/2006JD007340), 2006.

Paulsen, D., Dommen, J., Kalberer, M., Prévôt, A. S. H., Richter, R., Sax, M., Steinbacher, M., Weingartner, E., and Baltensperger, U.: Secondary Organic Aerosol Formation by Irradiation of 1,3,5-Trimethylbenzene–NO<sub>x</sub>–H<sub>2</sub>O in a New Reaction Chamber for Atmospheric Chemistry and Physics, *Environmental Science & Technology*, 39, 2668–2678, [10.1021/es0489137](https://doi.org/10.1021/es0489137), 2005.

Pierce, J. R., Engelhart, G. J., Hildebrandt, L., Weitkamp, E. A., Pathak, R. K., Donahue, N. M., Robinson, A. L., Adams, P. J., and Pandis, S. N.: Constraining Particle Evolution from Wall Losses, Coagulation, and Condensation–Evaporation in Smog-Chamber Experiments: Optimal Estimation Based on Size Distribution Measurements, *Aerosol Science and Technology*, 42, 1001–1015, [10.1080/02786820802389251](https://doi.org/10.1080/02786820802389251), 2008.

Poudel, S., Fiddler, M. N., Smith, D., Flurchick, K. M., and Bililign, S.: Optical Properties of Biomass Burning Aerosols: Comparison of Experimental Measurements and T-Matrix Calculations, *Atmosphere*, 8, 228, 2017.

Reid, J. S., Hobbs, P. V., Ferek, R. J., Blake, D. R., Martins, J. V., Dunlap, M. R., and Liousse, C.: Physical, chemical, and optical properties of regional hazes dominated by smoke in Brazil, *Journal of Geophysical Research: Atmospheres*, 103, 32059–32080, [10.1029/98JD00458](https://doi.org/10.1029/98JD00458), 1998.

Roberts, G., Wooster, M. J., and Lagoudakis, E.: Annual and diurnal african biomass burning temporal dynamics, *Biogeosciences*, 6, 849–866, [10.5194/bg-6-849-2009](https://doi.org/10.5194/bg-6-849-2009), 2009.

Roberts, G. J., and Wooster, M. J.: Fire Detection and Fire Characterization Over Africa Using Meteosat SEVIRI, *IEEE Transactions on Geoscience and Remote Sensing*, 46, 1200–1218, [10.1109/TGRS.2008.915751](https://doi.org/10.1109/TGRS.2008.915751), 2008.

Robinson, A. L., Donahue, N. M., Shrivastava, M. K., Weitkamp, E. A., Sage, A. M., Grieshop, A. P., Lane, T. E., Pierce, J. R., and Pandis, S. N.: Rethinking Organic Aerosols: Semivolatile Emissions and Photochemical Aging, *Science*, 315, 1259–1262, [10.1126/science.1133061](https://doi.org/10.1126/science.1133061), 2007.

ASTM G173-03 Reference Spectra Derived from SMARTS v. 2.9.2, access: December 21.

Rubasinghege, G., and Grassian, V. H.: Role(s) of adsorbed water in the surface chemistry of environmental interfaces, *Chemical Communications*, 49, 3071–3094, [10.1039/C3CC38872G](https://doi.org/10.1039/C3CC38872G), 2013.

Schick, S. F., Farraro, K. F., Fang, J., Nasir, S., Kim, J., Lucas, D., Wong, H., Balmes, J., Giles, D. K., and Jenkins, B.: An Apparatus for Generating Aged Cigarette Smoke for Controlled Human Exposure Studies, *Aerosol Science and Technology*, 46, 1246–1255, [10.1080/02786826.2012.708947](https://doi.org/10.1080/02786826.2012.708947), 2012.

Schultz, M. G., Heil, A., Hoelzemann, J. J., Spessa, A., Thonicke, K., Goldammer, J. G., Held, A. C., Pereira, J. M. C., and van het Bolscher, M.: Global wildland fire emissions from 1960 to 2000, *Global Biogeochemical Cycles*, 22, GB2002, [10.1029/2007GB003031](https://doi.org/10.1029/2007GB003031), 2008.

Shi, Y., Matsunaga, T., and Yamaguchi, Y.: High-Resolution Mapping of Biomass Burning Emissions in Three Tropical Regions, *Environmental Science & Technology*, 49, 10806–10814, [10.1021/acs.est.5b01598](https://doi.org/10.1021/acs.est.5b01598), 2015.

Singh, S., Fiddler, M. N., Smith, D., and Bililign, S.: Error Analysis and Uncertainty in the Determination of Aerosol Optical Properties Using Cavity Ring-Down Spectroscopy, Integrating Nephelometry, and the Extinction-Minus-Scattering Method, *Aerosol Science and Technology*, 48, 1345–1359, [10.1080/02786826.2014.984062](https://doi.org/10.1080/02786826.2014.984062), 2014.  
Singh, S., Fiddler, M. N., and Bililign, S.: Measurement of size-dependent single scattering albedo of fresh biomass burning aerosols using the extinction-minus-scattering technique with a combination of cavity ring-down spectroscopy and nephelometry, *Atmos. Chem. Phys.*, 16, 13491–13507, [10.5194/acp-16-13491-2016](https://doi.org/10.5194/acp-16-13491-2016), 2016.

Takekawa, H., Minoura, H., and Yamazaki, S.: Temperature dependence of secondary organic aerosol formation by photo-oxidation of hydrocarbons, *Atmospheric Environment*, 37, 3413–3424, [https://doi.org/10.1016/S1352-2310\(03\)00359-5](https://doi.org/10.1016/S1352-2310(03)00359-5), 2003.



Trump, E. R., Epstein, S. A., Riipinen, I., and Donahue, N. M.: Wall effects in smog chamber experiments: A model study, *Aerosol Science and Technology*, 50, 1180-1200, 10.1080/02786826.2016.1232858, 2016.

van der Werf, G. R., Randerson, J. T., Giglio, L., Collatz, G. J., Mu, M., Kasibhatla, P. S., Morton, D. C., DeFries, R. S., Jin, Y., and van Leeuwen, T. T.: Global fire emissions and the contribution of deforestation, savanna, forest, agricultural, and peat fires (1997–2009), *Atmos. Chem. Phys.*, 10, 11707-11735, 10.5194/acp-10-11707-2010, 2010.

Wang, J., Doussin, J. F., Perrier, S., Perraudin, E., Katrib, Y., Pangui, E., and Picquet-Varrault, B.: Design of a new multi-phase experimental simulation chamber for atmospheric photochemical, aerosol and cloud chemistry research, *Atmos. Meas. Tech.*, 4, 2465-2494, 10.5194/amt-4-2465-2011, 2011.

Wang, X., Liu, T., Bernard, F., Ding, X., Wen, S., Zhang, Y., Zhang, Z., He, Q., Lü, S., Chen, J., Saunders, S., and Yu, J.: Design and characterization of a smog chamber for studying gas-phase chemical mechanisms and aerosol formation, *Atmos. Meas. Tech.*, 7, 301-313, 10.5194/amt-7-301-2014, 2014.

Weitkamp, E. A., Sage, A. M., Pierce, J. R., Donahue, N. M., and Robinson, A. L.: Organic Aerosol Formation from Photochemical Oxidation of Diesel Exhaust in a Smog Chamber, *Environmental Science & Technology*, 41, 6969-6975, 10.1021/es070193r, 2007.

Wu, S., Lü, Z., Hao, J., Zhao, Z., Li, J., Takekawa, H., Minoura, H., and Yasuda, A.: Construction and characterization of an atmospheric simulation smog chamber, *Advances in Atmospheric Sciences*, 24, 250-258, 10.1007/s00376-007-0250-3, 2007.

Yokelson, R. J., Crounse, J. D., DeCarlo, P. F., Karl, T., Urbanski, S., Atlas, E., Campos, T., Shinozuka, Y., Kapustin, V., Clarke, A. D., Weinheimer, A., Knapp, D. J., Montzka, D. D., Holloway, J., Weibring, P., Flocke, F., Zheng, W., Toohey, D., Wennberg, P. O., Wiedinmyer, C., Mauldin, L., Fried, A., Richter, D., Walega, J., Jimenez, J. L., Adachi, K., Buseck, P. R., Hall, S. R., and Shetter, R.: Emissions from biomass burning in the Yucatan, *Atmos. Chem. Phys.*, 9, 5785-5812, 10.5194/acp-9-5785-2009, 2009.

Zauscher, M. D., Wang, Y., Moore, M. J. K., Gaston, C. J., and Prather, K. A.: Air Quality Impact and Physicochemical Aging of Biomass Burning Aerosols during the 2007 San Diego Wildfires, *Environmental Science & Technology*, 47, 7633-7643, 10.1021/es4004137, 2013.

Zhang, Q., Jimenez, J. L., Canagaratna, M. R., Ulbrich, I. M., Ng, N. L., Worsnop, D. R., and Sun, Y.: Understanding atmospheric organic aerosols via factor analysis of aerosol mass spectrometry: a review, *Analytical and Bioanalytical Chemistry*, 401, 3045-3067, 10.1007/s00216-011-5355-y, 2011.

Zhang, X., Cappa, C. D., Jathar, S. H., McVay, R. C., Ensberg, J. J., Kleeman, M. J., and Seinfeld, J. H.: Influence of vapor wall loss in laboratory chambers on yields of secondary organic aerosol, *Proceedings of the National Academy of Sciences*, 111, 5802-5807, 10.1073/pnas.1404727111, 2014.

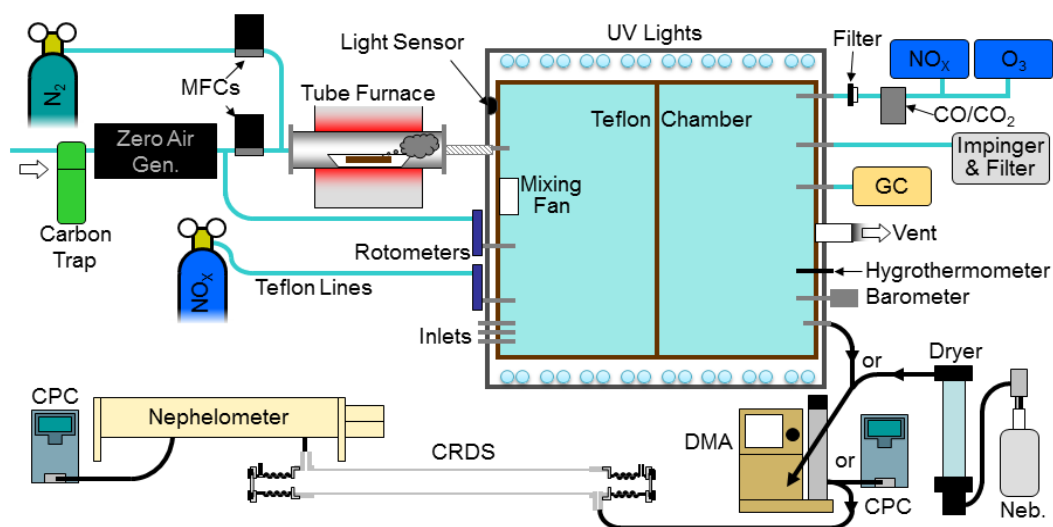


Figure 1: Schematics of the NCAT Chamber with all inputs and sampling lines, including analytical instruments and optical properties measurement facility (lasers not shown).

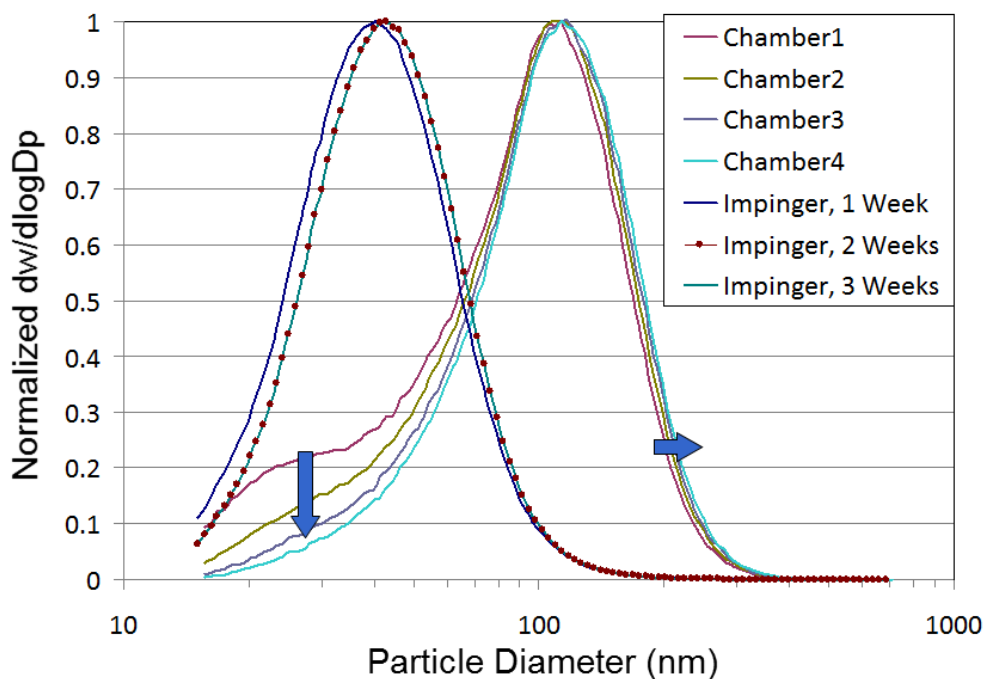


Figure 2: Normalized size distributions of fresh BB aerosol, measured directly from the chamber (right), compared to re-aerosolized BB aerosol, collected via impinger and stored in water (left). Note the shift and stability of the size distribution of impinged samples.

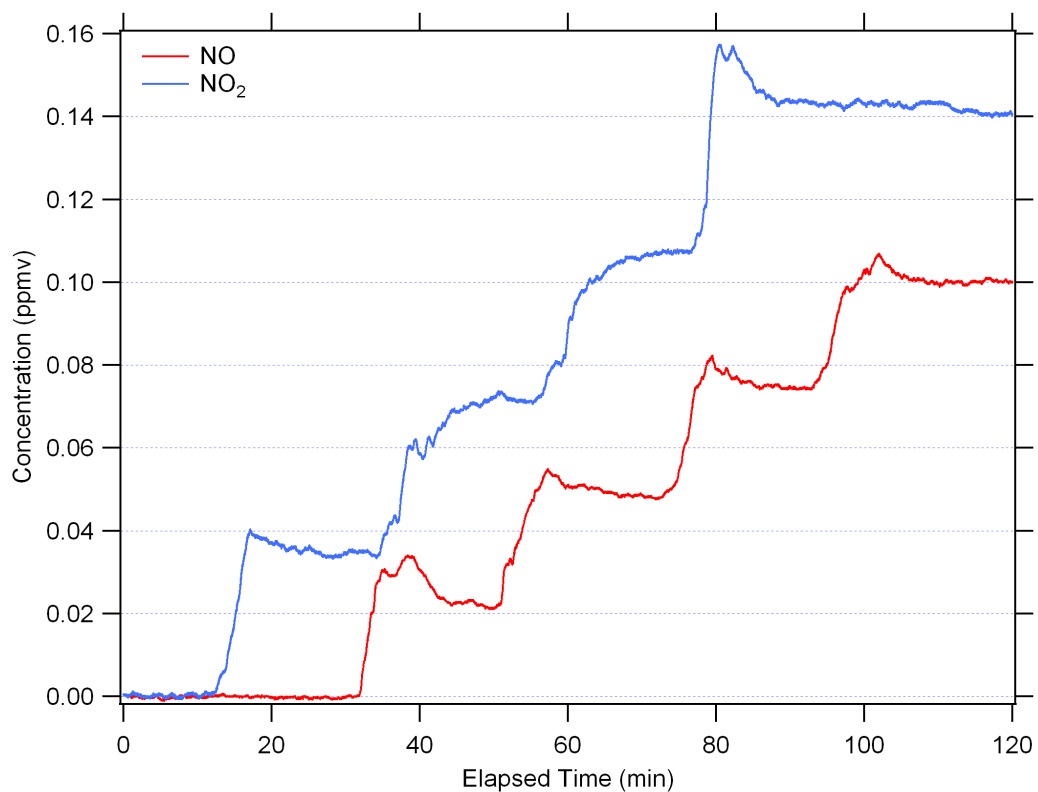


Figure 3: Injections and response (mixing) time for NO and NO<sub>2</sub>, done on different days.

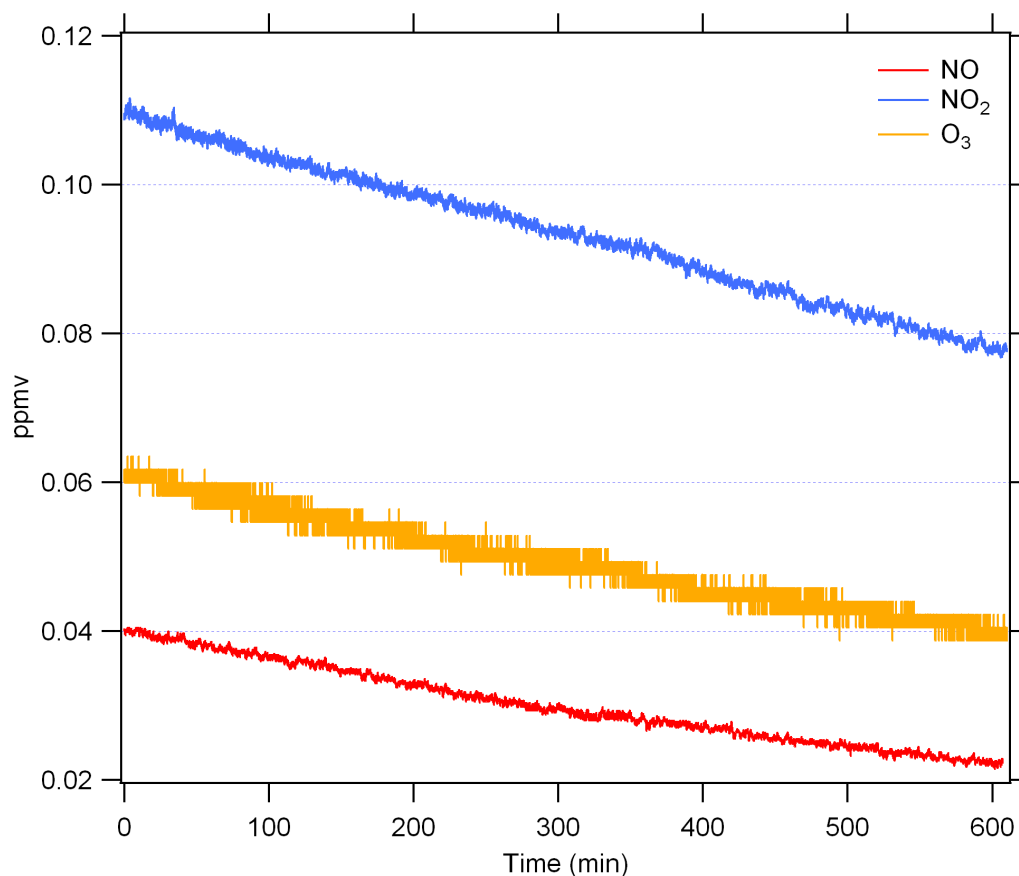
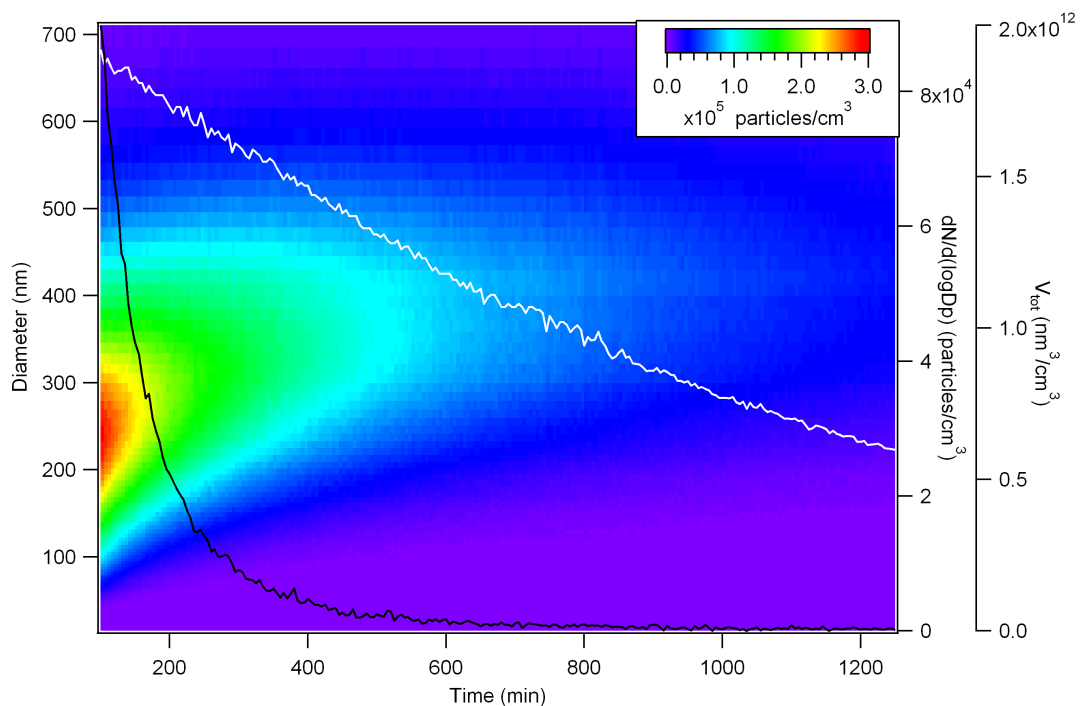
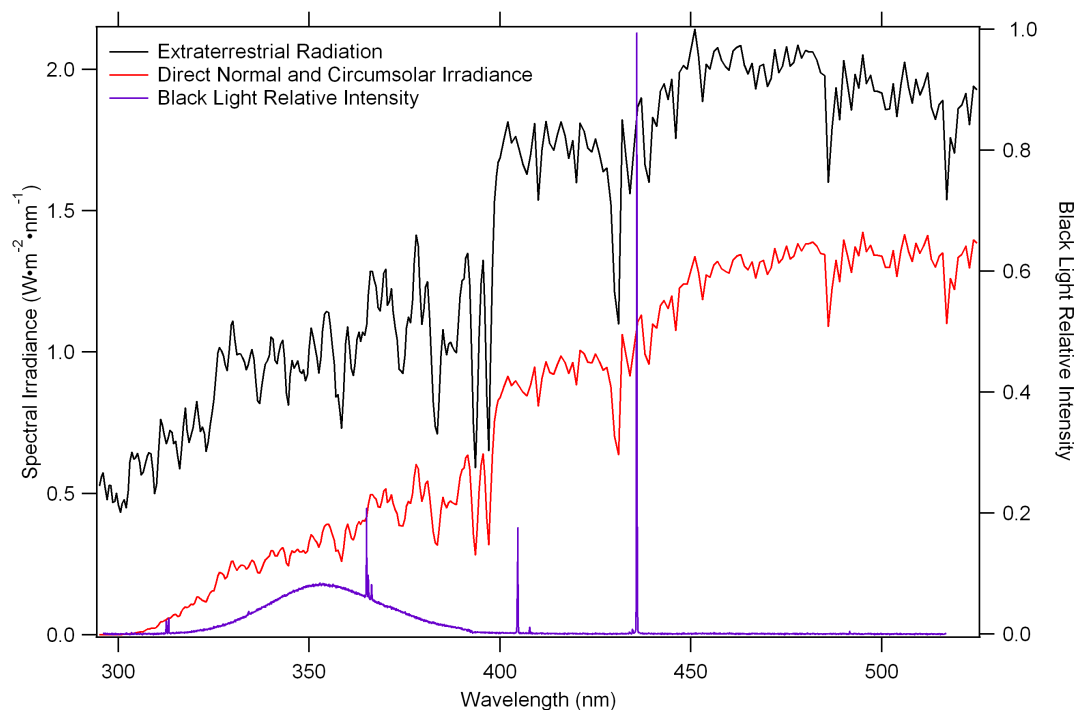


Figure 4: A typical example of an experiment shows the loss rate constant (wall loss plus dilution) was  $(10.120 \pm 0.031) \times 10^{-4}$ ,  $(7.796 \pm 0.033) \times 10^{-4}$ , and  $(6.487 \pm 0.164) \times 10^{-4} \text{ min}^{-1}$  for NO, NO<sub>2</sub>, and O<sub>3</sub>, respectively. This corresponds to lifetimes of 16.67, 21.31, and 25.69 hours, respectively. The results in Table 2 are averages of several runs.



**Figure 5:** The number density size distribution of pine combustion over time (background) with particle loss at  $D_p = 100$  nm (black) and aerosol volume loss (white). The line at  $t = 450$  shows where the size distribution stabilizes



**Figure 6:** Comparison of the solar spectrum to the UV lamps in our chamber. Extraterrestrial radiation (black) and direct normal and circumsolar irradiance (red) is from the ASTM G173-03 reference spectra derived from SMARTS v. 2.9.2 (RReDC). UV lamps (blue) were measured in our laboratory using Ocean Optics spectrometer (HR2000+ GRATING #H12, with wavelength range 296.0–516.8 nm, a ILX-511B detector with UV window, and 10 microns slit width.

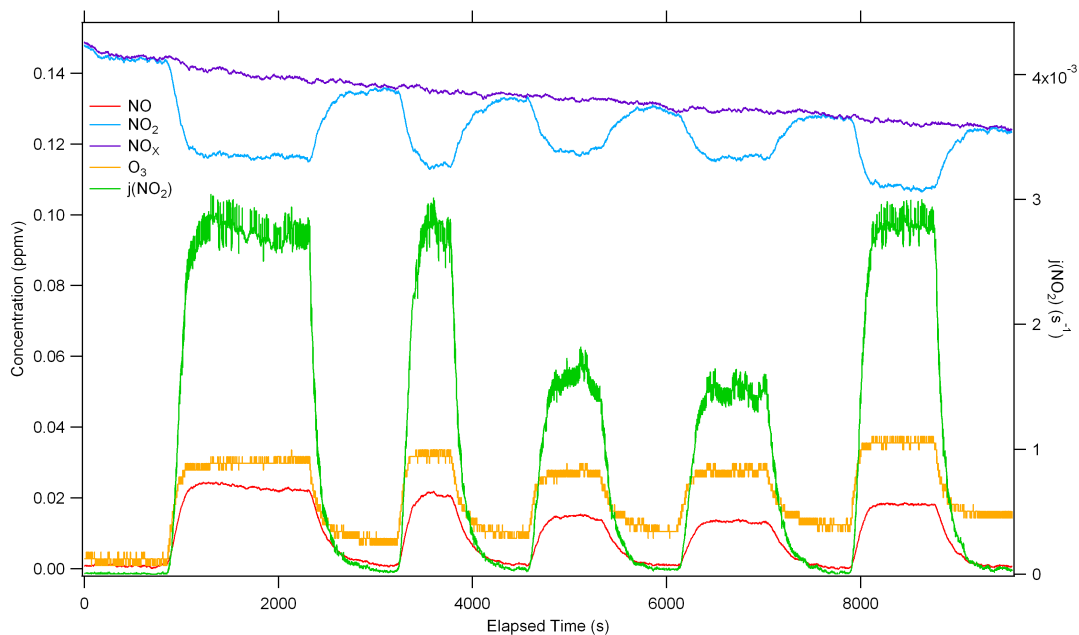


**Figure 7:** A plot of the  $\text{NO}_2$  photolysis rate constant ( $j$ ) against concentrations of  $\text{NO}$ ,  $\text{NO}_2$ , and  $\text{O}_3$ . The largest first, second, and last  $j$  peaks correspond to all lights turned on (100%), with  $j$  values of  $(2.73 \pm 0.09) \times 10^{-3} \text{ s}^{-1}$ ,  $(2.78 \pm 0.11) \times 10^{-3} \text{ s}^{-1}$ , and  $(2.78 \pm 0.07) \times 10^{-3} \text{ s}^{-1}$ , respectively. The third and fourth peaks represent the door side and window side of the chamber, respectively, and only use half of the lights (50%), with  $j$  values of  $(1.56 \pm 0.09) \times 10^{-3} \text{ s}^{-1}$  and  $(1.45 \pm 0.07) \times 10^{-3} \text{ s}^{-1}$ , respectively.

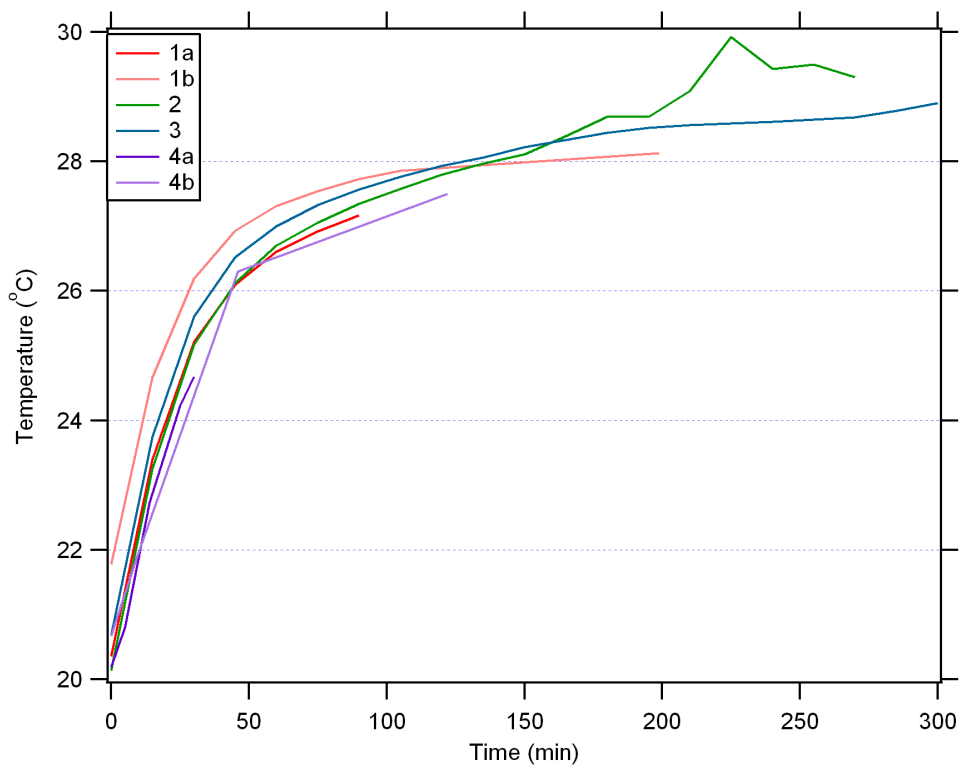


Figure 8: Temperature profile of the chamber. Runs 1b and 4b were done on the same day as runs 1a and 4a, respectively, with initial temperatures higher for 1b and 4b than 1a and 4a.



**Table I.** List and description of analytical instrumentation used with the NCAT chamber.

Species/Variable	Instrument	Range	Detection Limit	Accuracy
NO/NO <sub>2</sub>	Nitrogen Oxides Analyzer, Monitor Labs, Model 8340, San Diego, CA, USA	0–1 ppm	2 ppb	±1 ppb
O <sub>3</sub>	U.V. Photometric O <sub>3</sub> Analyzer, Thermo Electron, Model 49, Franklin, MA, USA	0–1 ppm	2 ppb	±2.5 ppb
Hydrocarbons	Analytical Gas Chromatograph, Carle Instruments, Model 211	0–1 ppm typical	2–10 ppb	±2 to 10 ppb
CO <sub>2</sub> /CO	Portable IAQ Meter, AZ Instrument, Model 77597, Taichung City, Taiwan	CO <sub>2</sub> : 0–5000 ppm CO: 0–1000 ppm	1 ppm	CO <sub>2</sub> : ±30 ppm ±5 % of reading CO: ±10 ppm (≤ 100 ppm), ±10 % (between 101–500 ppm), ±20 % (> 500 ppm)
Pressure	Omega Instruments, Part #PX309- 015AI, Norwalk, CT, USA	-15 to 50 psig	N/A	±0.25 % BSL, max
Temperature/Relative Humidity/Dew Point	Traceable Products, Model 4085, Webster, TX, USA	Temp: -40 °C to 104.4 °C RH: 5–95 %	Temp: 0.01 RH: 0.01 %	Temp: ±0.4 °C (0–40 °C), ±1 °C otherwise RH: ±1.5 %



**Table 2. Chamber characteristics and decay rates in  $\text{min}^{-1}$  for several comparable indoor atmospheric chambers. KNU: Kyungpook National University (Babar, 2016). TU: Tsinghua University (Shan, 2007). GIG-CAS: Guabgzhon Institute of Geochemistry-Chinese Academy of Science (Wang, 2014). Ilmari University of Eastern Finland (Leskinen, 2015).**

Chamber	Volume $\text{m}^3$	Surface to Volume Ratio $\text{m}^{-1}$	NO $\text{min}^{-1}$	NO <sub>2</sub> $\text{min}^{-1}$	O <sub>3</sub> $\text{min}^{-1}$	$k_{dep}$ (100 nm) $\text{min}^{-1}$	$j_{NO_2}$ $\text{min}^{-1}$
NCAT	9.0	2.90	(7.40±0.01) $\times 10^{-4}$	(3.47±0.01) $\times 10^{-4}$	(5.91±0.08) $\times 10^{-4}$	(2.46±0.11) $\times 10^{-3}$	0.165±0.005
KNU	7	3.09	$3.78 \times 10^{-4}$	$4.48 \times 10^{-4}$	$6.47 \times 10^{-4}$	$3.96 \times 10^{-3}$	0.17
TU	2	5	$3.38 \times 10^{-4}$	$4.17 \times 10^{-4}$	$6.07 \times 10^{-4}$	$2.6 \times 10^{-3}$	0.23
GIG-CAS	30	2.07	$1.41 \times 10^{-4}$	$1.39 \times 10^{-4}$	$1.31 \times 10^{-4}$	$3.83 \times 10^{-3}$	0.49
Ilmari	29	1.97				$7.5 \times 10^{-4}$	0.132